




Article

Voltage-Tunable UVC–UVB Dual-Band Metal–Semiconductor–Metal Photodetector Based on Ga₂O₃/MgZnO Heterostructure by RF Sputtering

Jie-Si Jheng ¹, Chun-Kai Wang ^{2,*}, Yu-Zung Chiou ², Sheng-Po Chang ¹ and Shouu-Jinn Chang ¹

¹ Institute of Microelectronics and Department of Electrical Engineering, National Cheng Kung University, Tainan 70101, Taiwan; jayseajean@gmail.com (J.-S.J.); changsp@mail.ncku.edu.tw (S.-P.C.); changsj@mail.ncku.edu.tw (S.-J.C.)

² Department of Electronic Engineering, Southern Taiwan University of Science and Technology, Tainan 71005, Taiwan; yzchiou@stust.edu.tw

* Correspondence: ckwang@stust.edu.tw

Received: 22 September 2020; Accepted: 16 October 2020; Published: 17 October 2020



Abstract: Dual-band metal–semiconductor–metal (MSM) photodetectors (PDs) with a Ga₂O₃/MgZnO heterostructure were fabricated by radio frequency (RF) sputtering, which can detect ultraviolet C (UVC) and ultraviolet B (UVB) bands individually by controlling different bias voltages. A PD with the annealing temperature of Ga₂O₃ at 600 °C can improve the crystal quality of Ga₂O₃ thin film and exhibit the least persistent photoconductivity (PPC) effect. However, a PD with the annealing temperature of Ga₂O₃ at 600 °C cannot achieve a voltage-tunable dual-band characteristic. On the contrary, the PD without annealing can suppress the carriers from the bottom layer of MgZnO thin film at a lower bias voltage of 1 V. At this time, the peak responsivity at 250 nm was mainly dominated by the top layer of Ga₂O₃ thin film. Then, as the bias voltage increased to 5 V, the peak detection wavelength shifted from 250 (UVC) to 320 nm (UVB). In addition, the PD with a 25 nm–thick SiO₂ layer inserted between Ga₂O₃ and MgZnO thin film can achieve a broader operating bias voltage range for dual-band applications.

Keywords: Ga₂O₃; MgZnO; dual-band PD; UVB; UVC; voltage-tunable

1. Introduction

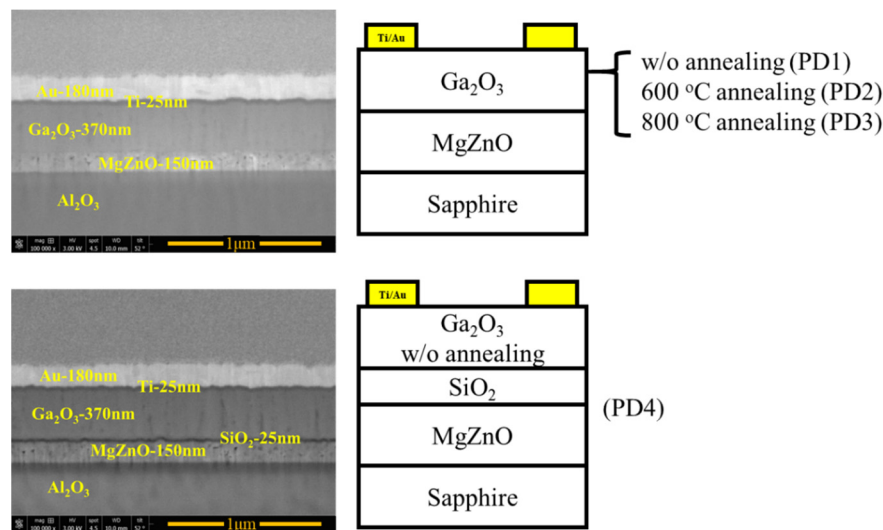
For solid-state lighting, ultraviolet (UV) light has unique applications compared with visible light. UV light has been widely used in disinfection, biotechnology, medical science, military, and space technology. According to the different applications, UV light can be divided into three sub-bands: ultraviolet A (UVA) (320–400 nm), ultraviolet B (UVB) (280–320 nm), and ultraviolet C (UVC) (200–280 nm). Wide-bandgap semiconductor materials, such as Ga₂O₃, BeZnO, ZnO, Sr₂Nb₃O₁₀, Al_xGa_{1-x}N, and Mg_xZn_{1-x}O, have been generally used to design and fabricate UV photodetectors (PDs) [1–11]. Al_xGa_{1-x}N based on GaN series materials has been developed for decades and is widely used in near-UV PDs. However, for deep-UV PDs, the Al composition of AlGaN is generally over 35% to modulate the detection wavelength of PDs. This higher Al composition in AlGaN can induce significant leakage current from defects through the path [12–14]. Mg_xZn_{1-x}O, a representative ternary alloy of wide-bandgap semiconductor material, has gained popularity for fabricating UVB and UVC optoelectronic devices due to its energy bandgap, ranging from 3.37 (ZnO) to 7.8 eV (MgO) [15–18]. However, the crystal structure of Mg_xZn_{1-x}O can be changed from wurtzite to cubic as the Mg composition is increased. Therefore, it is challenging to grow a single crystalline Mg_xZn_{1-x}O, especially for wurtzite Mg_xZn_{1-x}O with more than 36% Mg composition [19]. A Ga₂O₃ material with

an intrinsic wide-bandgap range of 4.2–4.9 eV has been considered as an ideal candidate for fabricating UVC PDs, especially in solar-blind applications [20–30].

The Ga₂O₃ series heterojunction UV PDs have been previously analyzed. Hung et al. reported a Ga₂O₃/AlGaIn/GaN heterostructure UV three-band PD, and the absorbed wavelength ranges from UVA to UVC [31]. Nakagomi et al. fabricated a deep-UV PD based on the β -Ga₂O₃/GaN heterojunction, and the highest responsivity was located at 240 nm [32]. Zhao et al. designed a solar-blind PD based on a ZnO/Ga₂O₃ core-shell heterostructured microwire that exhibited high responsivity at 0 V and different absorbed wavelengths, at 0, −2, and 2 V [20]. Despite these findings, the ZnO series material was chosen in studies based on its advantage of a simple process. However, the studies on Ga₂O₃/MgZnO heterojunction UV PDs are still unclear. Furthermore, the devices used in the previous studies had a dual-band absorbed wavelength; however, the central absorbed wavelength of PDs could not be changed while the bias voltage was varied. In another previous study, MgZnO/SiO₂/ZnO heterojunction dual-band UV PDs were successfully grown and fabricated, allowing users to choose the central absorption wavelength from UVB to UVA at different operating bias voltages, and the central absorption wavelength shift can achieve a value of 55 nm [33]. In this study, Ga₂O₃/MgZnO heterojunction dual-band UVC and UVB PDs were manufactured by RF sputtering, and the impact of the Ga₂O₃ annealing temperatures was investigated. In addition, the influence of the SiO₂ insertion layer on the Ga₂O₃ and MgZnO thin films was also investigated.

2. Materials and Methods

In this study, acetone, isopropanol, and deionized water were successively used to clean the sapphire substrate using an ultrasonic cleaner (Delta-D150, Taiwan) for 30 min. After the typical cleaning process, a 150 nm-thick MgZnO thin film was grown on the c-plane sapphire substrate, using an RF magnetron sputter system (KD-SPUTTER, Kao Duen Technology Corp., New Taipei City, Taiwan). The MgZnO target had an Mg content of 20%. Ar and oxygen (O₂) gases were used as sputtering gases. The Ar flow rate, O₂ flow rate, chamber pressure, and RF power were maintained at 25 sccm, 3 sccm, 10 mTorr, and 80 W, respectively. After growing the MgZnO thin film, the samples were annealed at 700 °C, in a tube furnace (ADVANCE RIKO, RHL-P series P610CP, Yokohama, Japan), in air, for 30 min. Then, parts of the samples were divided to grow a 25 nm-thick SiO₂ on an MgZnO thin film at 300 °C by using a plasma-enhanced chemical vapor deposition (PECVD) system (Oxford Plasmalab System 100, Bristol, UK). This was followed by growing a 370 nm-thick Ga₂O₃ thin film on the MgZnO or SiO₂ thin film by an RF magnetron sputter system, at room temperature. The Ar flow rate, O₂ flow rate, chamber pressure, and RF power were 98 sccm, 2 sccm, 5 mTorr, and 80 W, respectively. Finally, the Ga₂O₃/MgZnO heterojunction structure was annealed at 600 or 800 °C. Figure 1 presents all the proposed designs of Ga₂O₃/MgZnO heterojunction PDs. The following two types of structures were used in this study: Ga₂O₃ with or without annealing temperatures at 600 or 800 °C in air for 30 min (labeled as PD1, PD2, and PD3), and an unannealed Ga₂O₃ thin film with a 25 nm-thick SiO₂ insertion layer (labeled as PD4). The devices with a metal–semiconductor–metal (MSM) structure consisting of two interdigitated contact electrodes. The length, width, and finger space were 1000, 100, and 200 μ m, respectively. A Ti/Au (25 nm/180 nm) metal was subsequently deposited as electrodes, using an electron beam evaporator. Figure 2 presents the cross-sectional line scan of the energy-dispersive X-ray spectroscopy (EDX) analysis for Ga₂O₃/MgZnO heterojunction UV PDs with and without a 25 nm-thick SiO₂ insertion layer. Different stacked materials, including Ti, Au, Ga₂O₃, MgZnO, Al₂O₃, and SiO₂, were observed. The details of the growth parameter are shown in Figure 1.



| Sample | Ga ₂ O ₃ Annealed Temperature (°C) | MgZnO Annealed Temperature (°C) | 25 nm-thick SiO ₂ Inserting Layer by PECVD |
|--------|----------------------------------------------------------|---------------------------------|-------------------------------------------------------|
| PD1 | – | 700 | No |
| PD2 | 600 | 700 | No |
| PD3 | 800 | 700 | No |
| PD4 | – | 700 | Yes |

Figure 1. Schematic structures and scanning electron microscope (SEM) cross-section of Ga₂O₃/MgZnO heterojunction UV PDs with and without different annealing temperatures and a 25 nm-thick SiO₂ inserting layer. The table shows the detail of the parameters of PD1–PD4.

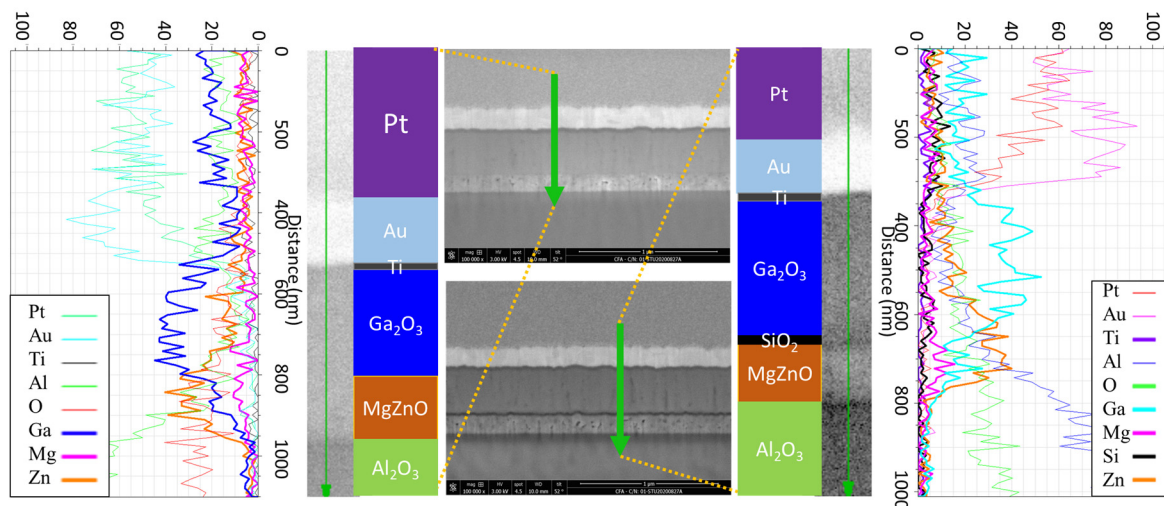


Figure 2. Line scanning EDX analysis of Ga₂O₃/MgZnO heterojunction UV PDs without and with a 25 nm-thick SiO₂ inserting layer.

The dark current characteristics of these PDs were analyzed by using an semiconductor parameter analyzer (Agilent HP-4156C, Santa Clara, CA, USA) with a cascade micro-chamber and cascade DCP 100 series low-noise electrical performance probe. An analysis of the spectral responsivity measurements by a Monochromator (HORIBA/JOBIN YVON/SPEX TRIAX 320 system, Kyoto, Japan) was also performed with a 300 W Xe arc lamp as a light source and a standard synchronous detection scheme.

3. Results and Discussion

3.1. The Photo and Dark Current

Figure 3 presents the photo- and dark-current characteristics of the fabricated MSM PDs, with and without different annealing temperatures of the Ga_2O_3 thin film, which were measured by using a 300 W Xe arc lamp as a light source. It was found that the dark currents of PD1, PD2, and PD3 were 1.72×10^{-6} , 3.15×10^{-8} , and 8.81×10^{-4} A at 5 V, respectively. The PD2 with an annealing temperature of 600 °C exhibited the lowest dark current, which is attributed to the improvement of the thin film's crystal quality after annealing. The grain size of the Ga_2O_3 thin film increased as the annealing temperature increased for scanning electron microscopy (not shown here). The Ga_2O_3 thin film deposited by sputtering was originally in an amorphous state. After the annealing process, the amorphous state can change to the polymorphic state, which indicates that more crystal structures can reorganize. Therefore, the number of grain boundaries can decrease as the annealing temperature increases, that is, the dark current of the sample can be reduced at high annealing temperatures due to the reduction of defects and healing of leakage current paths. However, the dark current apparently increased for PD3 with an annealing temperature of Ga_2O_3 at 800 °C. Ju et al. reported that MgZnO thin films exhibited better crystal quality at an annealing temperature of 750 °C. When the annealing temperature of the MgZnO thin film was raised to 850 °C, the full-width half-maximum (FWHM) of the X-ray diffraction (XRD) signal rapidly increased owing to phase separation [34]. In this study, the annealing temperature of the MgZnO thin film was 700 °C, to obtain a high crystal quality before the growth of the Ga_2O_3 thin film. However, the Ga_2O_3 thin film grown on the MgZnO thin film was subsequently annealed at a temperature of 800 °C, which can result in the destruction of the MgZnO crystalline structure. In addition, Chikoidze et al. proposed that the annealing temperature of Ga_2O_3 thin films above 700 °C in air or oxygen ambient would lead to the creation of oxygen vacancies (V_O) due to the out-diffusion of oxygen atoms from the Ga_2O_3 thin film. This generation of V_O would lead to an additional source of free electrons and an n-type conductivity enhancement [35]. This is why PD3 with an annealing temperature of Ga_2O_3 at 800 °C had a reverse effect on the dark-current characteristic. In contrast, the photo-to-dark-current ratios (PDCRs) of PD1, PD2, and PD3 at 5 V were 30.75, 132.18, and 1.33, respectively. The PD2 with an annealing temperature of Ga_2O_3 at 600 °C demonstrated the highest PDCR, owing to the improvement of the Ga_2O_3 thin film quality and maintenance of the MgZnO crystalline quality at the same time.

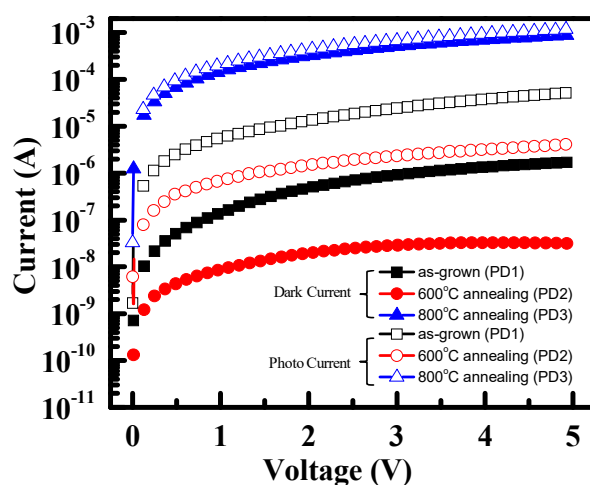


Figure 3. Photo and dark currents of $\text{Ga}_2\text{O}_3/\text{MgZnO}$ heterojunction UV PDs, with and without different annealing temperatures.

3.2. Persistent Photoconductivity Effect

Figure 4a presents the time-dependent current analysis of the Ga₂O₃/MgZnO heterojunction UV MSM PDs, with and without different annealing temperatures, using an Agilent HP-4156C semiconductor parameter analyzer, and the excitation light source used a 300 W Xe lamp with an electronic shutter to stop the excitation. Oxide semiconductor materials usually have a persistent photoconductivity (PPC) effect, which is a phenomenon in which carriers are captured by defects, and they persist for an extended period after the termination of light excitation. Therefore, carriers trapped at defects can be released slowly, and the carrier transport to the electrodes is delayed, which can affect the transient behaviors of the photocurrent in these types of PDs. Namely, the PPC effect is closely related to the defect density of the PDs. As shown in Figure 4a, the photocurrent of PD2 with an annealing temperature of Ga₂O₃ at 600 °C dropped faster than those of the other two because of the smaller PPC effect. Then, the curves can be fitted by the following equation [36,37]:

$$I(t) = A_1 e^{\left(\frac{-t}{\tau_1}\right)} + A_2 e^{\left(\frac{-t}{\tau_2}\right)} \quad (1)$$

where A_1 and A_2 are constants, t is the measured time, and τ_1 and τ_2 are the time constants. The τ_1 of PD1, PD2, and PD3 was calculated to be 5.2, 1.78, and 8.28 s, respectively. Apparently, the PD2 with an annealing temperature of Ga₂O₃ at 600 °C achieved the best time response characteristic. This is because the defect density of Ga₂O₃ at the grain boundary can be significantly reduced without damaging the quality of the MgZnO thin film; therefore, the PPC effect has a lesser influence. This time-response characteristic is consistent with the aforementioned result of the dark current. Figure 4b presents the I - V characteristics of PD2 under UV ON/OFF cycles. The PD2 with an annealing temperature of Ga₂O₃ at 600 °C exhibited sufficient cyclicity under periodic illumination, indicating that the device could be reproduced.

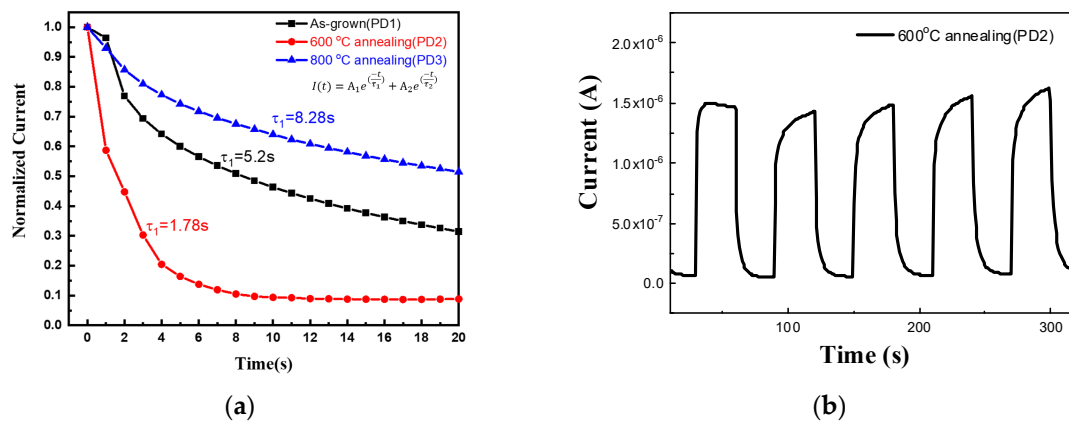


Figure 4. (a) Time-dependent current analysis of Ga₂O₃/MgZnO heterojunction UV PDs; (b) I - V characteristics of PD2, under UV ON/OFF cycles.

3.3. Voltage-Tunable the Central Wavelength of Spectrum

Figure 5a–c presents the normalized responsivities of PD1, PD2, and PD3 at different bias voltages, respectively. As shown in Figure 5a, it was found that the wavelengths of peak responsivity of PD1 at bias voltages of 1 and 5 V were approximately 250 and 320 nm, respectively. As the bias voltage of PD1 increased, the peak detection wavelength of PD1 could shift from 250 (UVC) to 320 nm (UVB). The absorbed wavelength of Ga₂O₃ and MgZnO is 250 and 320 nm, respectively. It is evident that a dual-band PD can be achieved by controlling the bias voltages. This is because, when the bias voltage is small, the electric field of the MSM PD can only be distributed to the shallower thin-film area. At this time, only the electron–hole pairs generated in the Ga₂O₃ thin film on the top layer of the MSM PD can be swept to the electrodes by the lower electric field. Then, when the bias voltage is

increased, the electric field can be distributed to cover the Ga_2O_3 and MgZnO thin-film area. Moreover, the internal quantum efficiency of the MgZnO thin film was higher than that of the Ga_2O_3 thin film. Therefore, in the case of the higher bias voltage, the peak responsivity of PD was mainly dominated by the MgZnO thin film. Next, as shown in Figure 5b, it can be observed that the same voltage-tunable dual-band characteristic as PD1 in Figure 5a cannot be achieved. Irrespective of the small or large bias voltage, the peak of the response was mainly dominated by the MgZnO thin film, and it can only detect the UVB band. The relevant description and explanation are shown in the schematic diagram of the energy band in Figure 5d. The left image in Figure 5d is a schematic diagram of the energy band of PD1. Because the Ga_2O_3 thin film of PD1 without an annealing process has a higher resistance and a lower carrier concentration, a higher potential energy barrier can be generated at the heterojunction of Ga_2O_3 and MgZnO , to prevent electrons and holes from the bottom layer of the MgZnO thin film at lower bias voltages. Therefore, such a result can assist in achieving a voltage-tunable dual-band PD. However, the right image in Figure 5d is a schematic diagram of the energy band of PD2. Owing to the annealing process, the resistance of the Ga_2O_3 thin film of PD2 decreases, and the carrier concentration increases, which reduces the potential energy barrier between the heterojunction of Ga_2O_3 and MgZnO . It is indicated that this lower barrier height cannot effectively keep off the carriers, despite lower bias voltages. This result makes it easy for electrons and holes from the bottom layer of the MgZnO thin film to transit the barrier height and reach the electrodes. Finally, in Figure 5c, the annealing process at 800°C caused the phase separation of the MgZnO thin film and the increase of oxygen vacancies in the Ga_2O_3 thin film, as indicated in the previous paragraph. Therefore, PD3 with an annealing temperature of 800°C exhibited the worst response characteristics and could not achieve dual-band detection.

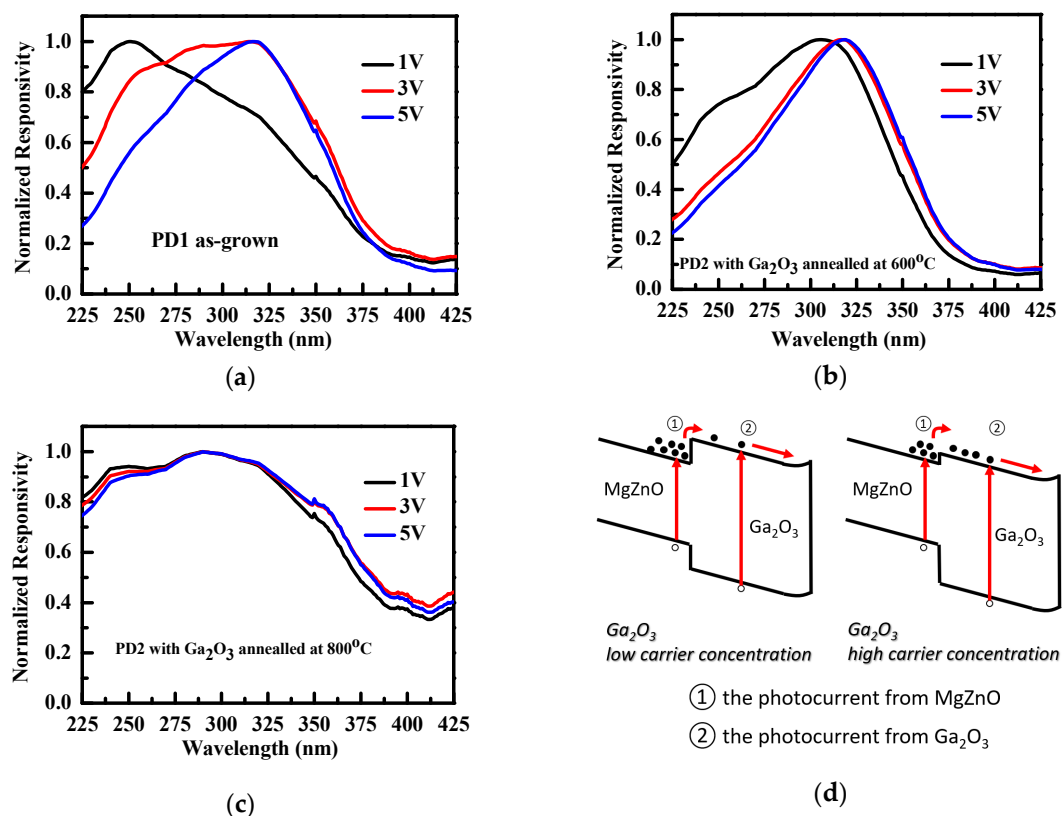


Figure 5. Normalized responsivities of the fabricated PDs with different Ga_2O_3 annealing temperatures: (a) as-grown, (b) at 600°C , and (c) at 800°C . (d) The schematic diagram of the $\text{Ga}_2\text{O}_3/\text{MgZnO}$ energy band as a Ga_2O_3 n-type oxide semiconductor with a lower and higher concentration.

3.4. Extend the Operating Bias Voltage of UVB

Although voltage-tunable UVC–UVB dual-band MSM PDs, which can shift the central detection wavelength to over 70 nm by using different bias voltages, were successfully fabricated, the bias voltages of the PDs for detecting UVC and UVB were too close, limiting the operating voltage range of the devices. Therefore, the structure of PD4 was also designed with a 25 nm-thick SiO₂ layer inserted between Ga₂O₃ and the MgZnO thin film to conduct this concept. As shown in Figure 6a, the peak responsivity of PD4 with a 25 nm-thick SiO₂ insertion layer was still dominated by the Ga₂O₃ thin film, to detect the UVC range at a bias voltage of 3 V, despite the bias voltage being as high as 7 V. It was not until the bias voltage reached 24 V that the peak responsivity of PD4 could be turned to be dominated by the MgZnO thin film to detect the UVB range. Considering these results, a 25 nm-thick SiO₂ inserting layer had a significant effect and could achieve a broader operating bias voltage range. Figure 6b presents the schematic energy band diagram of the electron transport mechanism for PD4 with a SiO₂ inserting layer. SiO₂ has a significantly high potential energy barrier compared to the original heterojunction of Ga₂O₃/MgZnO. As shown in Figure 6b, there are only two ways for the electron to pass through this high barrier. One is across, by a significantly high bias voltage, and the other is directly through the tunneling effect. This is why PD4 cannot detect the UVB band until the bias condition of 24 V. In addition, owing to the influence of the tunneling effect, the response values of PD4 in the UVB range at a bias voltage of 7 V were higher than those of 3 V. Namely, according to this design concept, a suitable voltage-tunable dual-band photodetector can be fabricated by using different SiO₂ thicknesses, without affecting the quality of the Ga₂O₃ and MgZnO thin films. Moreover, the performance of this study is compared with state-of-the-art reports, as shown in Table 1. Although dual-band PDs have been reported several times in previous studies, only the design proposed in this study has the ability to turn the central wavelength of the spectrum from UVC to UVB by different bias voltages.

Table 1. Comparison of results with those of state-of-the-art reports.

| Reference | Type | Responsivity (A/W) | External Quantum Efficiency (EQE) (%) | PDCR | Wavelength of Responsivity (nm) | Voltage-tunable the Central Wavelength of Spectrum |
|-----------------|-----------------|---------------------------------------------|---------------------------------------|--------------------------------------|---------------------------------|----------------------------------------------------|
| This work (PD1) | MSM (dual-band) | 1 V:0.14 m (250 nm) 5 V:2.07 m (320 nm) | 1 V:0.07 (250 nm) 5 V:0.8 (320 nm) | 5 V:30.75 | 250 (1 V), 320 (5 V) | Yes |
| [38] | MSM (dual-band) | 5 V:11.85 | 5 V:5070 | 5 V:1141 | 300, 350 | No |
| [39] | MSM (dual-band) | 35 V:13.1 | – | 20 V:~10 ⁴ | 325, 365 | No |
| [40] | MSM | 5 V:0.1 | 5 V:0.49 | 5 V:2 × 10 ⁴ | 254 | No |
| [41] | PN | 4.27 | 1.97 | 9153 | 254 | No |
| [42] | PN | 3 V:88.5 m (238 nm) 3 V:1.24 m (1030 nm) | – | 3 V:740 (238 nm) 3 V:38 (1030 nm) | 238, 1030 | No |

MSM = metal–semiconductor–metal.

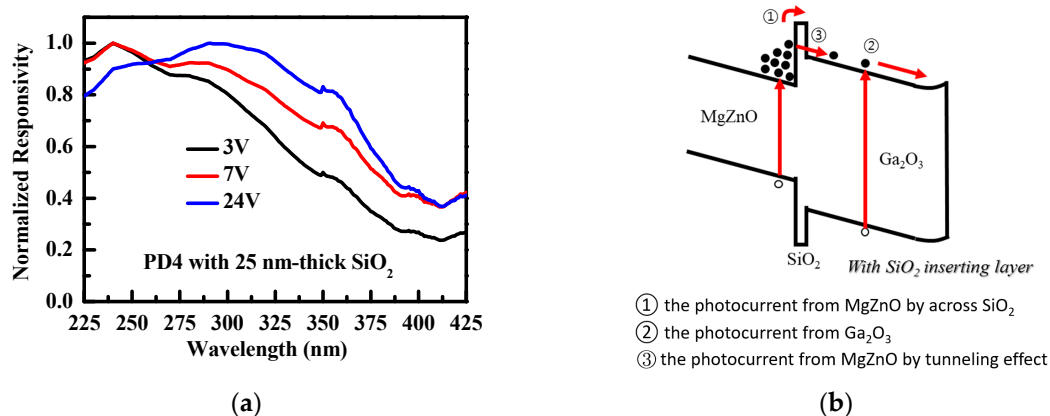


Figure 6. (a) Normalized responsivity of the fabricated PD with a 25 nm-thick SiO₂ inserting layer. (b) Schematic of the Ga₂O₃/SiO₂/MgZnO energy band.

4. Conclusions

In summary, Ga₂O₃/MgZnO heterostructure MSM PDs were fabricated by RF sputtering, and these fabricated PDs could detect the UVC and UVB dual-band individually by controlling different bias voltages. Although the crystal quality of the Ga₂O₃ thin film, the dark current of PD, PDCR of PD, and PCC effect can be improved by an annealing temperature of 600 °C, it cannot achieve a voltage-tunable dual-band characteristic. This was because the PD with an annealing temperature of Ga₂O₃ at 600 °C had a lower potential energy barrier between the Ga₂O₃ and MgZnO heterojunctions. Otherwise, the PD without annealing had a higher heterojunction barrier and could suppress the carriers from the bottom layer of the MgZnO thin film to cross this potential barrier at a lower bias voltage of 1 V. The peak responsivity was observed at 250 nm and was mainly dominated by the top layer of the Ga₂O₃ thin film. Next, as the bias voltage increased to 5 V, the peak detection wavelength shifted from UVC to UVB. Furthermore, a 25 nm-thick SiO₂ layer inserted between the Ga₂O₃ and MgZnO thin film of PD can achieve a broader operating voltage range for dual-band applications owing to the more effective blocking effect.

Author Contributions: Conceptualization, J.-S.J., C.-K.W., and Y.-Z.C.; investigation, J.-S.J.; methodology, C.-K.W., S.-P.C., and J.-S.J.; formal analysis, J.-S.J. and C.-K.W.; validation, J.-S.J. and S.-P.C.; resources, S.-J.C., Y.-Z.C., and C.-K.W.; writing—original draft, J.-S.J.; supervision, C.-K.W.; writing—review and editing, J.-S.J. and C.-K.W. All authors have read and agreed to the published version of the manuscript.

Funding: This research was funded by the Ministry of Science and Technology of Taiwan, under contract nos. MOST 106-2221-E-218-027 and MOST 107-2221-E-218-011.

Acknowledgments: This work was supported by the Ministry of Science and Technology of Taiwan, under contract nos. MOST 106-2221-E-218-027 and MOST 107-2221-E-218-011.

Conflicts of Interest: The authors declare no conflict of interest.

References

1. An, Y.; Chu, X.; Huang, Y.; Zhi, Y.; Guo, D.; Li, P.; Wu, Z.; Tang, W.H. Au plasmon enhanced high performance beta-Ga₂O₃ solar-blind photo-detector. *Prog. Nat. Sci. Mater. Int.* **2016**, *26*, 65–68. [\[CrossRef\]](#)
2. Chen, X.H.; Han, S.; Lu, Y.M.; Cao, P.J.; Liu, W.J.; Zeng, Y.X.; Jia, F.; Xu, W.Y.; Liu, X.K.; Zhu, D.L. High signal/noise ratio and high-speed deep UV detector on beta-Ga₂O₃ thin film composed of both (400) and (201) orientation beta-Ga₂O₃ deposited by the PLD method. *J. Alloys Compd.* **2018**, *747*, 869–878. [\[CrossRef\]](#)
3. Ariyawansa, G.; Rinzan, M.B.; Alevli, M.U.; Strassburg, M.; Dietz, N.; Perera, A.G.; Matsik, S.G.; Asghar, A.; Ferguson, I.T.; Luo, H.; et al. GaN/AlGaIn ultraviolet/infrared dual-band detector. *Appl. Phys. Lett.* **2006**, *89*, 91113. [\[CrossRef\]](#)
4. Korona, K.P.; Drabinska, A.; Caban, P.; Strupinski, W. Tunable GaN/AlGaIn ultraviolet detectors with built-in electric field. *J. Appl. Phys.* **2009**, *105*, 83712. [\[CrossRef\]](#)

5. Rana, V.S.; Rajput, J.K.; Pathak, T.K.; Purohit, L.P. Multilayer MgZnO/ZnO thin films for UV photodetectors. *J. Alloys Compd.* **2018**, *764*, 724–729. [\[CrossRef\]](#)
6. Takagi, T.; Tanaka, H.; Fujita, S.; Fujita, S. Molecular beam epitaxy of high magnesium content single-phase wurzite $\text{Mg}_x\text{Zn}_{1-x}\text{O}$ alloys ($x \approx 0.5$) and their application to solar-blind region photodetectors. *Jpn. J. Appl. Phys.* **2003**, *42*, L401. [\[CrossRef\]](#)
7. Su, L.X.; Chen, H.Y.; Xu, X.J.; Fang, X.S. Novel BeZnO based self-powered dual-color UV photodetector realized via a one-step fabrication method. *Laser Photonics Rev.* **2017**, *11*, 1700222. [\[CrossRef\]](#)
8. Chang, S.Y.; Chang, M.T.; Yang, Y.P. Enhanced responsivity of GaN metal-semiconductor-metal (MSM) photodetectors on GaN substrate. *IEEE Photonics J.* **2017**, *9*, 1–7. [\[CrossRef\]](#)
9. Hu, K.; Teng, F.; Zheng, L.X.; Yu, P.P.; Zhang, Z.M.; Chen, H.Y.; Fang, X.S. Binary response Se/ZnO p-n heterojunction UV photodetector with high on/off ratio and fast speed. *Laser Photonics Rev.* **2017**, *11*, 1600257. [\[CrossRef\]](#)
10. Li, S.Y.; Zhang, Y.; Yang, W.; Liu, H.; Fang, X.S. 2D perovskite $\text{Sr}_2\text{Nb}_3\text{O}_{10}$ for high-performance UV photodetectors. *Adv. Mater.* **2020**, *32*, 1905443. [\[CrossRef\]](#)
11. Li, Z.; Xu, Y.; Zhang, J.; Cheng, Y.; Chen, D.; Feng, Q.; Xu, S.R.; Zhang, Y.C.; Hang, J.C.; Hao, Z.Y.; et al. Flexible solar-blind Ga_2O_3 ultraviolet photodetectors with high responsivity and photo-to-dark current ratio. *IEEE Photonics J.* **2019**, *11*, 1–9. [\[CrossRef\]](#)
12. Walker, D.; Kumar, V.; Mi, K.; Sandvik, P.; Kung, P.; Zhang, X.H.; Razeghi, M. Solar-blind AlGaIn photodiodes with very low cutoff wavelength. *Appl. Phys. Lett.* **2000**, *76*, 403–405. [\[CrossRef\]](#)
13. Tut, T.; Gokkavas, M.; Inal, A.; Ozbay, E. $\text{Al}_x\text{Ga}_{1-x}\text{N}$ -based avalanche photodiodes with high reproducible avalanche gain. *Appl. Phys. Lett.* **2007**, *90*, 163506. [\[CrossRef\]](#)
14. Parish, G.; Keller, S.; Kozodoy, P.; Ibbetson, J.P.; Marchand, H.; Fini, P.T.; Fleischer, S.B.; DenBaars, S.P.; Mishra, U.K.; Tarsa, E.J. High-performance (Al,Ga)N-based solar-blind ultraviolet *p-i-n* detectors on laterally epitaxially overgrown GaN. *Appl. Phys. Lett.* **1999**, *75*, 247–249. [\[CrossRef\]](#)
15. Ohtomo, A.; Kawasaki, M.; Koida, T.; Masubuchi, K.; Koinuma, H.; Sakurai, Y.; Yoshida, Y.; Yasuda, T.; Segawa, Y. $\text{Mg}_x\text{Zn}_{1-x}\text{O}$ as a II-VI widegap semiconductor alloy. *Appl. Phys. Lett.* **1998**, *72*, 2466–2468. [\[CrossRef\]](#)
16. Kang, J.W.; Choi, Y.S.; Kim, B.H.; Goo Kang, C.; Hun Lee, B.; Tu, C.W.; Park, S.J. Ultraviolet emission from a multi-layer graphene/MgZnO/ZnO light-emitting diode. *Appl. Phys. Lett.* **2014**, *104*, 51120. [\[CrossRef\]](#)
17. Chen, H.; Yu, P.; Zhang, Z.; Teng, F.; Zheng, L.; Hu, K.; Fang, X. Ultrasensitive self-powered solar-blind deep-ultraviolet photodetector based on all-solid-state polyaniline/MgZnO bilayer. *Small* **2016**, *12*, 5809–5816. [\[CrossRef\]](#)
18. Schleife, A.; Eisenacher, M.; Rödl, C.; Fuchs, F.; Furthmüller, J.; Bechstedt, F. Ab initio description of heterostructural alloys: Thermodynamic and structural properties of $\text{Mg}_x\text{Zn}_{1-x}\text{O}$ and $\text{Cd}_x\text{Zn}_{1-x}\text{O}$. *Phys. Rev. B* **2010**, *81*, 245210. [\[CrossRef\]](#)
19. Shiau, J.S.; Brahma, S.; Liu, C.P.; Huang, J.L. Ultraviolet photodetectors based on MgZnO thin film grown by RF magnetron sputtering. *Thin Solid Film* **2016**, *620*, 170–174. [\[CrossRef\]](#)
20. Zhao, B.; Wang, F.; Chen, H.; Zheng, L.; Su, L.; Zhao, D.; Fang, X. An ultrahigh responsivity (9.7 mA W^{-1}) self-powered solar-blind photodetector based on individual ZnO- Ga_2O_3 heterostructures. *Adv. Funct. Mater.* **2017**, *27*, 1700264. [\[CrossRef\]](#)
21. Qiao, B.; Zhang, Z.; Xie, X.; Li, B.; Li, K.; Chen, X.; Zhao, H.F.; Liu, K.W.; Liu, L.; Shen, D.Z. Avalanche gain in metal-semiconductor-metal Ga_2O_3 solar-blind photodiodes. *J. Phys. Chem. C* **2019**, *123*, 18516–18520. [\[CrossRef\]](#)
22. Guo, X.C.; Hao, N.H.; Guo, D.Y.; Wu, Z.P.; An, Y.H.; Chu, X.L.; Li, L.H.; Li, P.G.; Lei, M.; Tang, W.H. Beta- Ga_2O_3 /p-Si heterojunction solar-blind ultraviolet photodetector with enhanced photoelectric responsivity. *J. Alloy. Compd.* **2016**, *660*, 136–140. [\[CrossRef\]](#)
23. Chen, Y.C.; Lu, Y.J.; Liu, Q.; Lin, C.N.; Guo, J.; Zang, J.H.; Tian, Y.Z.; Shan, C.X. Ga_2O_3 photodetector arrays for solar-blind imaging. *J. Mater. Chem. C* **2019**, *7*, 2557–2562. [\[CrossRef\]](#)
24. Qian, L.X.; Zhang, H.F.; Lai, P.T.; Wu, Z.H.; Liu, X.Z. High-sensitivity beta- Ga_2O_3 solar-blind photodetector on high-temperature pretreated c-plane sapphire substrate. *Opt. Mater. Express* **2017**, *7*, 3643–3653. [\[CrossRef\]](#)
25. Wang, X.; Chen, Z.; Guo, D.; Zhang, X.; Wu, Z.; Li, P.; Tang, W. Optimizing the performance of a beta- Ga_2O_3 solar-blind UV photodetector by compromising between photoabsorption and electric field distribution. *Opt. Mater. Express* **2018**, *8*, 2918–2927. [\[CrossRef\]](#)

26. Yang, C.; Liang, H.; Zhang, Z.; Xia, X.; Tao, P.; Chen, Y.; Zhang, H.Q.; Shen, R.S.; Luo, Y.M.; Du, G.T. Self-powered SBD solar-blind photodetector fabricated on the single crystal of beta-Ga₂O₃. *Rsc Adv.* **2018**, *8*, 6341–6345. [\[CrossRef\]](#)
27. Patil-Chaudhari, D.; Ombaba, M.; Oh, J.Y.; Mao, H.; Montgomery, K.H.; Lange, A.; Mahajan, S.; Woodall, J.M.; Islam, M.S. Solar Blind photodetectors enabled by nanotextured beta-Ga₂O₃ films grown via oxidation of GaAs substrates. *IEEE Photonics J.* **2017**, *9*, 1–7. [\[CrossRef\]](#)
28. Rafique, S.; Han, L.; Zhao, H.P. Thermal annealing effect on β-Ga₂O₃ thin film solar blind photodetector heteroepitaxially grown on sapphire substrate. *Phys. Status Solidi A* **2017**, *214*, 1700063. [\[CrossRef\]](#)
29. Qian, L.X.; Liu, X.Z.; Sheng, T.; Zhang, W.L.; Li, Y.R.; Lai, P.T. Beta-Ga₂O₃ solar-blind deep-ultraviolet photodetector based on a four-terminal structure with or without Zener diodes. *Aip Adv.* **2016**, *6*, 45009. [\[CrossRef\]](#)
30. Liu, S.B.; Chang, S.J.; Chang, S.P.; Chen, C.H. An Amorphous (Al_{0.12}Ga_{0.88})₂O₃ Deep Ultraviolet Photodetector. *IEEE Photonics J.* **2020**, *12*, 1–8. [\[CrossRef\]](#)
31. Huang, Z.D.; Weng, W.Y.; Chang, S.J.; Chiu, C.J.; Hsueh, T.J.; Wu, S.L. Ga₂O₃/AlGaIn/GaN Heterostructure Ultraviolet Three-Band Photodetector. *IEEE Sens. J.* **2013**, *13*, 3462–3467. [\[CrossRef\]](#)
32. Nakagomi, S.; Sato, T.A.; Takahashi, Y.; Kokubun, Y. Deep ultraviolet photodiodes based on the beta-Ga₂O₃/GaN heterojunction. *Sens. Actuators A Phys.* **2015**, *232*, 208–213. [\[CrossRef\]](#)
33. Jheng, J.S.; Wang, C.K.; Chiou, Y.Z.; Chang, S.P.; Chang, S.J. MgZnO/SiO₂/ZnO metal-semiconductor-metal dual-band UVA and UVB photodetector with different MgZnO thicknesses by RF magnetron sputter. *Jpn. J. Appl. Phys.* **2020**, *59*, SDDF04. [\[CrossRef\]](#)
34. Ju, Z.G.; Shan, C.X.; Yang, C.L.; Zhang, J.Y.; Yao, B.; Zhao, D.X.; Shen, D.Z.; Fan, X.W. Phase stability of cubic Mg_{0.55}Zn_{0.45}O thin film studied by continuous thermal annealing method. *Appl. Phys. Lett.* **2009**, *94*, 101902. [\[CrossRef\]](#)
35. Chikoidze, E.; Sartet, C.; Mohamed, H.; Madaci, I.; Tchelidze, T.; Modreanu, M.; Vales-Castro, P.; Rubio, C.; Arnold, C.; Sallet, V.; et al. Enhancing the intrinsic p-type conductivity of the ultra-wide bandgap Ga₂O₃ semiconductor. *J. Mater. Chem. C* **2019**, *7*, 10231–10239. [\[CrossRef\]](#)
36. Zeng, X.R.; Sang, H.Y.; Cai, Z.G.; Zheng, J.S.; Lu, Y.J.; Gao, Y.L. Time-resolved photoluminescence study of Ga_{0.52}In_{0.48}P alloys. *Eur. Phys. J. B* **2002**, *28*, 145.
37. Reddeppa, M.; Park, B.G.; Majumder, S.; Kim, Y.H.; Oh, J.E.; Kim, S.G.; Kim, D.; Kim, M.-D. Hydrogen passivation: A proficient strategy to enhance the optical and photoelectrochemical performance of InGaIn/GaN single-quantum-well nanorods. *Nanotechnology* **2020**, *31*, 475201. [\[CrossRef\]](#) [\[PubMed\]](#)
38. Liu, H.Y.; Hou, F.Y.; Chu, H.S. Mg_{0.35}Zn_{0.65}O/Al/ZnO Photodetectors With Capability of Identifying Ultraviolet-A/Ultraviolet-B. *IEEE Trans. Electron Devices* **2020**, *67*, 2812. [\[CrossRef\]](#)
39. Li, M.; Zhao, M.; Jiang, D.; Li, Q.; Shan, C.; Zhou, X.; Duan, Y.H.; Wang, N.; Sun, J.M. Optimizing the performance of ZnO/Au/MgZnO/SiO₂ sandwich structured UV photodetectors by surface plasmons in Ag nanoparticles. *Appl. Phys. A* **2020**, *126*, 310. [\[CrossRef\]](#)
40. Yu, J.; Wang, Y.; Li, H.; Huang, Y.; Tang, W.; Wu, Z. Tailoring the solar-blind photoresponse characteristics of beta-Ga₂O₃ epitaxial films through lattice mismatch and crystal orientation. *J. Phys. D.* **2020**, *53*, 24LT01. [\[CrossRef\]](#)
41. Yu, J.; Yu, M.; Wang, Z.; Yuan, L.; Huang, Y.; Zhang, L.; Zhang, Y.M.; Jia, R.X. Improved photoresponse performance of self-powered beta-Ga₂O₃/NiO heterojunction UV photodetector by surface plasmonic effect of Pt nanoparticles. *IEEE Trans. Electron Devices* **2020**, *67*, 3199–3204. [\[CrossRef\]](#)
42. He, T.; Li, C.; Zhang, X.; Ma, Y.; Cao, X.; Shi, X.; Sun, C.; Li, J.S.; Song, L.; Zeng, C.H.; et al. Metalorganic chemical vapor deposition heteroepitaxial beta-Ga₂O₃ and black phosphorus Pn heterojunction for solar-blind ultraviolet and infrared dual-band photodetector. *Phys. Status Solidi A* **2020**, *217*, 1900861. [\[CrossRef\]](#)

Publisher's Note: MDPI stays neutral with regard to jurisdictional claims in published maps and institutional affiliations.



© 2020 by the authors. Licensee MDPI, Basel, Switzerland. This article is an open access article distributed under the terms and conditions of the Creative Commons Attribution (CC BY) license (<http://creativecommons.org/licenses/by/4.0/>).